Multicolour single-molecule tracking of mRNA interactions with RNP granules

Stephanie L. Moon [ID][1,2,5], Tatsuya Morisaki [ID][3,5], Anthony Khong[1,2], Kenneth Lyon[3], Roy Parker [ID][1,2]* and Timothy J. Stasevich [ID][3,4]*

Ribonucleoprotein (RNP) granules are non-membrane-bound organelles that have critical roles in the stress response[1,2], maternal messenger RNA storage[3], synaptic plasticity[4], tumour progression[5,6] and neurodegeneration[7–9]. However, the dynamics of their mRNA components within and near the granule surface remain poorly characterized, particularly in the context and timing of mRNAs exiting translation. Herein, we used multicolour single-molecule tracking to quantify the precise timing and kinetics of single mRNAs as they exit translation and enter RNP granules during stress. We observed single mRNAs interacting with stress granules and P-bodies, with mRNAs moving bidirectionally between them. Although translating mRNAs only interact with RNP granules dynamically, non-translating mRNAs can form stable, and sometimes rigid, associations with RNP granules with stability increasing with both mRNA length and granule size. Live and fixed cell imaging demonstrated that mRNAs can extend beyond the protein surface of a stress granule, which may facilitate interactions between RNP granules. Thus, the recruitment of mRNPs to RNP granules involves dynamic, stable and extended interactions affected by translation status, mRNA length and granule size that collectively regulate RNP granule dynamics.

To simultaneously visualize and quantify the exit of single mRNAs from translation and their dynamic interactions with ribonucleoprotein (RNP) granules in living cells, we adapted the newly developed nascent chain tracking technique[10]. The translation of individual mRNAs labelled with fluorescent MS2 coat protein (MCP–HaloTag with Janelia Fluor 646 (JF646) dye[11]) was monitored via the binding of fluorescent antibody fragments (Fab conjugated with the Cy3 dye) to epitopes at the N terminus of the nascent peptide (Fig. 1a). Thus, translating mRNAs were labelled with both MS2 coat protein (MCP) and Fab, whereas non-translating mRNAs were only labelled with MCP. By imaging these constructs in U-2 OS cells stably expressing the stress granule (SG) marker green fluorescent protein (GFP)–G3BP1[12], we could examine the translation status of single mRNAs during arsenite stress in relation to their interactions with individual SGs.

We first imaged cells at a lower temporal resolution (one volume every 3 min for 1 h) to determine the timing of translation repression during stress. To avoid background from single mature proteins and limit photobleaching, we lowered the laser powers so that only the mRNAs translating in polysomes were detectable. As the majority of translation output is thought to occur in polysomes, we
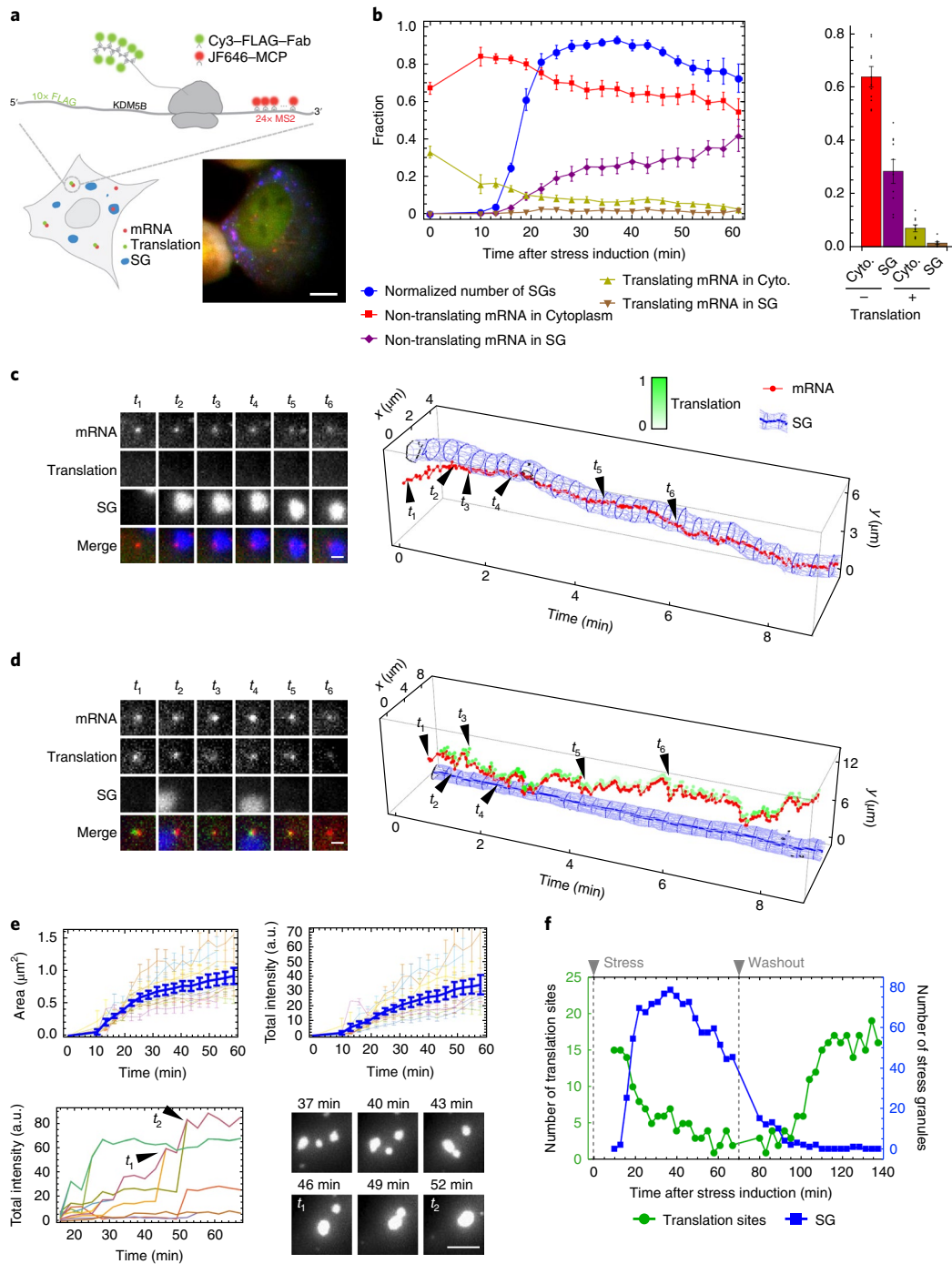
considered mRNAs without a detectable associated nascent peptide to be in a translationally repressed state. The translation of single KDM5B reporter mRNAs declined following stress, with SGs forming after 10 min of stress (Fig. 1b and Supplementary Video 1). The interaction of KDM5B mRNAs with SGs lagged slightly behind SG assembly, with about 30–40% of the mRNAs associating with SGs 40–60 min after the addition of arsenite, which is similar to what is predicted for endogenous KDM5B mRNAs from the SG transcriptome (~39%)[13]. Ninety-eight per cent of the KDM5B SG-associated mRNAs were translationally repressed, which implies that the repression of translation is a general prerequisite for the recruitment of mRNA to SGs. Surprisingly, 1–2% of SG-associated mRNAs retained nascent chains, suggesting that mRNAs can interact with SGs while still associated with polysomes. To verify these observations, we imaged samples at a higher temporal resolution (one volume every 2 s for 10 min) between 10 and 30 min post-stress, a period when both translating mRNAs and SGs are observed (Fig. 1b). This confirmed that most of the mRNAs entered SGs in a translationally repressed state (Fig. 1c and Supplementary Video 2). Between one and two per cent of the mRNAs interacting with SGs were associated with nascent chains, but these mRNAs only interacted with SGs transiently for a few seconds (Fig. 1d and Supplementary Video 3). Out of a total of 336 interactions detected, only two transcripts associated with nascent chains interacted with SGs for longer than two minutes (Supplementary Fig. 1 and Supplementary Video 3).

Translation repression positively correlates with the growth of SGs, which increases throughout the stress response[14–16]. Stress granules grew by both incremental accumulation of material and SG fusion (Fig. 1e). Incremental growth dominated during the early phases of stress, up to ~40 min post-stress, when the number and size of SGs continued to increase, whereas fusion events dominated at later time points, after ~40 min post-stress, when the number of SGs stopped increasing but SG size continued to increase. The growth of SGs also correlated with increased KDM5B mRNAs in SGs, which is consistent with mRNA recruitment contributing to SG growth.

During recovery from arsenite stress, SG disassembly (quantified as the number of individual SGs) occurred a few minutes before translation resumed in single cells (Fig. 1f, Supplementary Fig. 2 and Supplementary Video 4). We verified that these translating spots in the recovery phase were bona fide translating mRNAs by observing their disappearance following puromycin treatment (Supplementary Video 5). KDM5B mRNAs did not resume translation until the SGs had dissolved completely, suggesting that SGs

Fig. 1 | mRNAs are translationally repressed before entering SGs and resume translation following SG disassembly. a, Single mRNAs with 24× MS2 stem loops in the 3′ UTR were visualized with JF646–MCP (red) and translation was observed by anti-FLAG Cy3-Fab (green) binding to 10× FLAG tags in the N-terminal KDM5B open reading frame (ORF) in U-2 OS cells that express the SG marker GFP–G3BP1 (blue). Inset, a representative cell (from ten we analysed in detail in **b**) is shown. Scale bar, 10 μm. **b**, Simultaneous detection of mRNA localization, translation activity and SG formation in arsenite-stressed cells. Left, normalized number of SGs per cell (that is, fraction of the maximum number of SGs observed in each cell throughout the stress), fraction of cytoplasmic (Cyto.) non-translating and translating mRNAs, and fraction of SG-localized translating and non-translating mRNAs. Right, fraction of cytoplasmic or SG-localized translating or non-translating mRNAs at 40 min post-stress are shown. The mean ± s.e.m. is shown from n = 10 cells collected from three independent experiments. **c,d**, Representative images of single mRNAs (red), their translation activity (green) and SG (blue) interactions; scale bars, 1 μm (left); and graphical representations of the interactions with the intensity of translation foci represented as white–green (right). **c**, A representative long-term mRNA–SG interaction (>3 min) from 82 non-translating mRNAs tracked from n = 9 cells collected from three independent experiments. **d**, An example of transient translating mRNA–SG interactions from 334 translating mRNAs tracked from n = 9 cells collected from three independent experiments. **e**, Growth of SGs over time, as average SG size (upper left) and average SG intensity (upper right). Growth of individual SGs (lower left) with fusion events shown graphically (t_1 and t_2) and as a representative time series (lower right; scale bar, 5 μm). Mean ± s.e.m. is shown from n = 10 cells collected from three independent experiments. **f**, Representative data from a single cell (from n = 4 cells collected from two independent experiments) showing the resumption of translation after arsenite washout. The number of translation foci (green) and SGs (blue) during stress (0–70 min) and following washout (80–140 min) are shown. Source data are provided in Supplementary Table 2.

must disassemble before translation resumes during recovery from stress.

To determine how mRNAs interact with RNP granules, we measured the duration of individual SG interactions with mRNAs that encoded KDM5B, H2B or p300 (Fig. 2a,b). In all three cases, the probability that a SG–mRNA interaction lasted a set duration of time (that is, the interaction time survival probability) could be fit by a two-component model with fast interactions on the order of seconds and slow interactions on the order of many minutes (Fig. 2c,d). These results suggest that mRNAs frequently 'sample' SGs and occasionally enter a stable association.

Generally, three parameters influenced the nature of the SG–mRNA interactions. First, we compared the dynamic interactions of reporter mRNAs containing the KDM5B ORF (4,632 nt), the shorter H2B ORF (375 nt) or the longer p300 ORF (8,265 nt) with SGs by determining the dwell time of mRNAs in SGs and found that mRNA ORF length correlated with the duration of interactions with large SGs (Fig. 2c,d; $t_{slow}(H2B) = 1,400 \pm 300\,s$, $t_{slow}(KDM5B) = 2,000 \pm 300\,s$ and $t_{slow}(p300) = 3,700 \pm 600\,s$). We also observed that the duration of the slow interactions and the fraction of mRNAs engaged in slow interactions with SGs for the H2B, KDM5B and p300 mRNAs varied depending on the size of the SG. Larger SGs had more and longer stable interactions with mRNAs than smaller SGs (Fig. 2c,d and Supplementary Videos 6 and 7). The observation that longer mRNAs interact more stably with SGs explains why longer mRNAs were more likely to be highly enriched in the steady-state SG transcriptome[13,17]. Finally, we observed that KDM5B and p300 mRNAs still engaged with polysomes, as assessed by the detection of associated nascent peptides, and could interact with SGs transiently but did not engage in the stable interaction mode (Fig. 2e). We did not analyse translating H2B transcripts because they were more difficult to track due to their dim signals and low numbers per cell, even before stress[10]. Translating mRNAs in the cytoplasm moved slower than translationally repressed mRNAs (Fig. 4a), ruling out the possibility that the transient association of translating mRNAs with SGs was due to faster overall mobility. Together, these observations suggest that mRNA length, SG size and mRNA translation status are strongly correlated with mRNA partitioning into SGs, although there are probably other mRNP factors that influence the dynamics of mRNA–SG interactions.

To determine whether other RNP granules also exhibit bimodal interactions with mRNAs, we examined the dynamics of mRNA interactions with P-bodies (PBs), marked with mRFP–DCP1a in stressed U-2 OS cells that also expressed the SG marker GFP–G3BP1. We observed that H2B, KDM5B and p300 mRNAs all showed rapid and stable interactions with PBs (Fig. 3a), mRNA ORF length correlated with the duration of mRNA interaction with PBs, as p300 interacted most stably with PBs and H2B interacted most unstably with PBs (Fig. 3a,b), and the degree of stable interactions for all mRNAs analysed increased with the size of the PB (Fig. 3a,b and Supplementary Video 8). These observations indicate that mRNAs can dock and undock to SGs and PBs through transient interactions and in some cases form a stable set of interactions that 'locks' the mRNA into the granule for prolonged periods. A stable association could be more prevalent on longer mRNAs and in larger SGs and PBs due to increased sites for additional interactions. This model implies that the association of an mRNA with a granule can be influenced by *cis* or *trans* inputs that modify either the docking/undocking step or the rate of entry into a stable, locked interaction state, which is supported by the observation that knockdown of the RNA binding protein LARP1 can reduce the association of some mRNAs with PBs and SGs[18].

Non-translating mRNAs can accumulate in both SGs and PBs. A general model is that following translation repression, mRNAs first associate with SGs and then can be sorted for targeting to PBs[19]. In contrast, it has been proposed that mRNAs move from PBs to

SGs following glucose deprivation in yeast[20]. To determine whether there is a preferred movement of mRNAs between SGs and PBs, we simultaneously imaged SGs, PBs and KDM5B mRNAs during stress. We observed mRNA exchange between SGs and PBs in a bidirectional manner (Fig. 3c,d). These interactions included cases of mRNAs transitioning from a SG to a PB and back to a different SG within as little as ~30 s (Fig. 3c and Supplementary Video 9) and instances where the mRNA was localized between a PB and a SG for a few minutes (Fig. 3d and Supplementary Video 10). Transcripts were considered to be associated with a SG or PB when they moved with these granules over several frames (or at least 4 s). These rapid bidirectional movements between SGs and PBs indicate that there is no obligate path for mRNA movement between these granules, which also demonstrates that an individual mRNA with its associated proteins is capable of interacting with either SGs or PBs, or exchanges proteins that enables SG or PB interaction within seconds.

It has been proposed that SGs, and other RNP granules, are liquid-like compartments with components showing rapid diffusion within the compartment[21–24] and/or contain liquid-like areas surrounding densely compacted 'cores'[14,25]. Those mRNAs that were stably associated with RNP granules for many minutes adopted the motility of SGs (Fig. 4a) and could be observed at the surface or embedded within SGs (Fig. 4b). To examine the liquid-like nature of SGs, we examined the movement of mRNAs relative to one another within SGs. We observed two cases where the relative localization of mRNAs, as assessed by quantifying the distance and angle between three individual KDM5B mRNAs in one SG, remained relatively constant over time (Fig. 4b,c, Supplementary Figs. 3, 4 and Supplementary Videos 11, 12), consistent with limited movement of the mRNA within the larger assembly. Quantification revealed the intra-SG diffusion of mRNAs to be 280 times slower than the SG as a whole and over 1,600 times slower than free mRNAs within the cytoplasm (Fig. 4a). These observations demonstrate that SGs contain solid or gel-like components and mRNAs within large SGs can be rigidly positioned, with relatively limited movements of mRNAs.

Unexpectedly, we observed two cases where the MCP signal, which represents the 3′ end of a KDM5B mRNA, exited the SG and then returned to approximately the same position within the SG (yellow arrows, Fig. 4c; Supplementary Videos 11, 12 and Supplementary Figs. 3, 4). This observation suggested that the 3′ end of this mRNA might exit the GFP–G3BP1-marked portion of the SG while the remainder of the mRNA is still within the SG. Consistent with the body of an mRNA extending beyond the G3BP1-marked SG, we observed that endogenous RNAs that localize to SGs (*AHNAK* and *NORAD*) are often detected near, but not in, SGs in U-2 OS cells by single-molecule fluorescence in situ hybridization (smFISH; Fig. 4d) with the shorter *NORAD* RNA (~5 kb) closer to the periphery of a SG than the longer *AHNAK* RNA (18 kb). Furthermore, using smFISH probes to the 5′ or 3′ ends of the *AHNAK* mRNA, we observed that ~15% of ~1,000 *AHNAK* mRNAs were at the SG periphery with one end of the mRNA outside the SG while the other end co-localized with GFP–G3BP1, with an approximately two-fold bias for the 3′ end to be within the SG (Fig. 4e). These observations suggest that the surfaces of these membraneless organelles are not uniform and can have RNP extensions into the cytosol beyond boundaries as defined by protein components. Such surface extensions could thus provide a set of interactions to promote the fusion of smaller SGs and docking of SGs and PBs, which is consistent with our observations of individual mRNAs localizing between a PB and a SG for several minutes (Fig. 3d and Supplementary Video 10).

These experiments demonstrate that mRNAs interact with SGs and PBs in both stable and transient ways. In model assemblies, the exchange rates of components are related to both the strength of individual interactions and the valency, with more stable interactions occurring at higher valencies[26]. This suggests that the transient
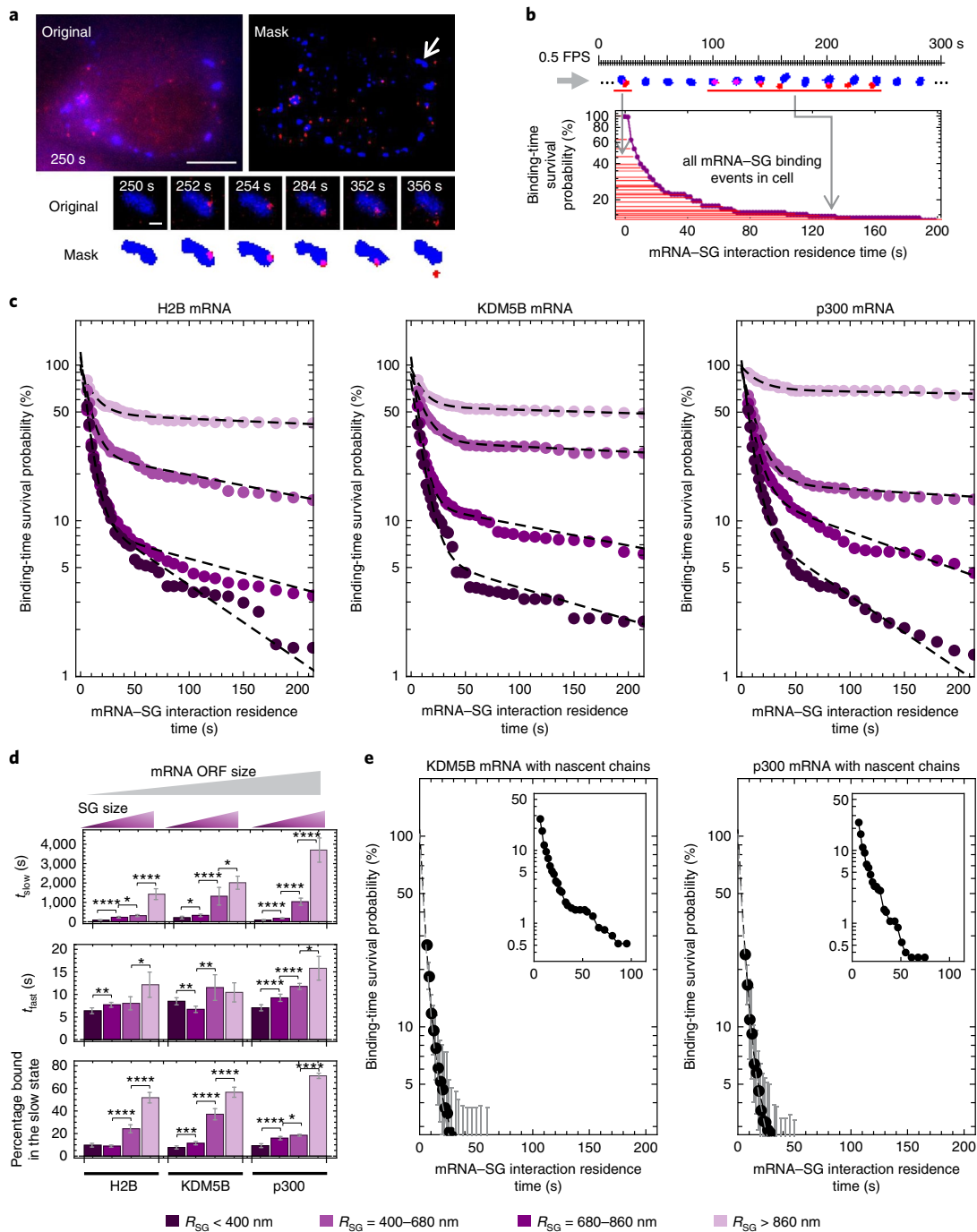
Fig. 2 | mRNAs interact transiently and stably with SGs. a, Determination of mRNA–SG interaction times. Representative image (from $n=9$ cells expressing KDM5B mRNA that we analysed in detail in **c**) showing mRNAs (red) and SGs (blue) (upper left; scale bar, 10 μm) and the masked image (upper right) with a representative mRNA–SG interaction (arrow) shown below (scale bar, 1 μm). **b**, Survival probability distribution of mRNA–SG interaction times (red) from one representative cell from $n=9$ cells expressing KDM5B mRNA that we analysed in detail in **c**. The diagram above the graph depicts representative masked mRNA (red) and SG (blue) interactions derived from imaging cells at 0.5 frames per second (FPS), with grey arrows indicating how these interactions are represented graphically below. **c**, The binding-time survival probability of H2B (left; data were calculated from 492 tracked SGs from $n=11$ cells collected from three independent experiments), KDM5B (middle; data were collected from 409 tracked SGs from $n=9$ cells collected from four independent experiments) and p300 (right; data were calculated from 824 tracked SGs from $n=16$ cells from four independent experiments) mRNA–SG interactions are shown partitioned by SG size (legend at the bottom). **d**, The extracted mRNA–SG interaction data in **c** were fit to a two-component model, resulting in average ($\pm$90% confidence interval (CI)) fitted slow and fast mRNA–SG interaction times, t_{slow} (top) and t_{fast} (middle), respectively, and percentage mRNA bound to SGs in the slow interaction mode ('slow state'). The fitted results are shown for H2B, KDM5B and p300 mRNAs for a given effective SG radius (R_{SG}) depicted as dotted lines. *$P<0.05$, **$P<0.01$, ***$P<0.005$, ****$P<0.001$ and d.f. $=44$; two-sided t-tests. The statistics source data can be found in Supplementary Table 2. Fitting was performed once to the collective data set shown in **c**. **e**, The average binding-time survival probability ($\pm$90% CI) of KDM5B (left; data were calculated from 326 tracked SGs from $n=9$ cells collected from three independent experiments) and p300 (right; data were calculated from 336 tracked SGs from $n=10$ cells collected from four independent experiments) mRNAs associated with nascent chains is shown with graphical insets showing the full distribution (adjusted x and y axes). The source data is provided in Supplementary Table 2.
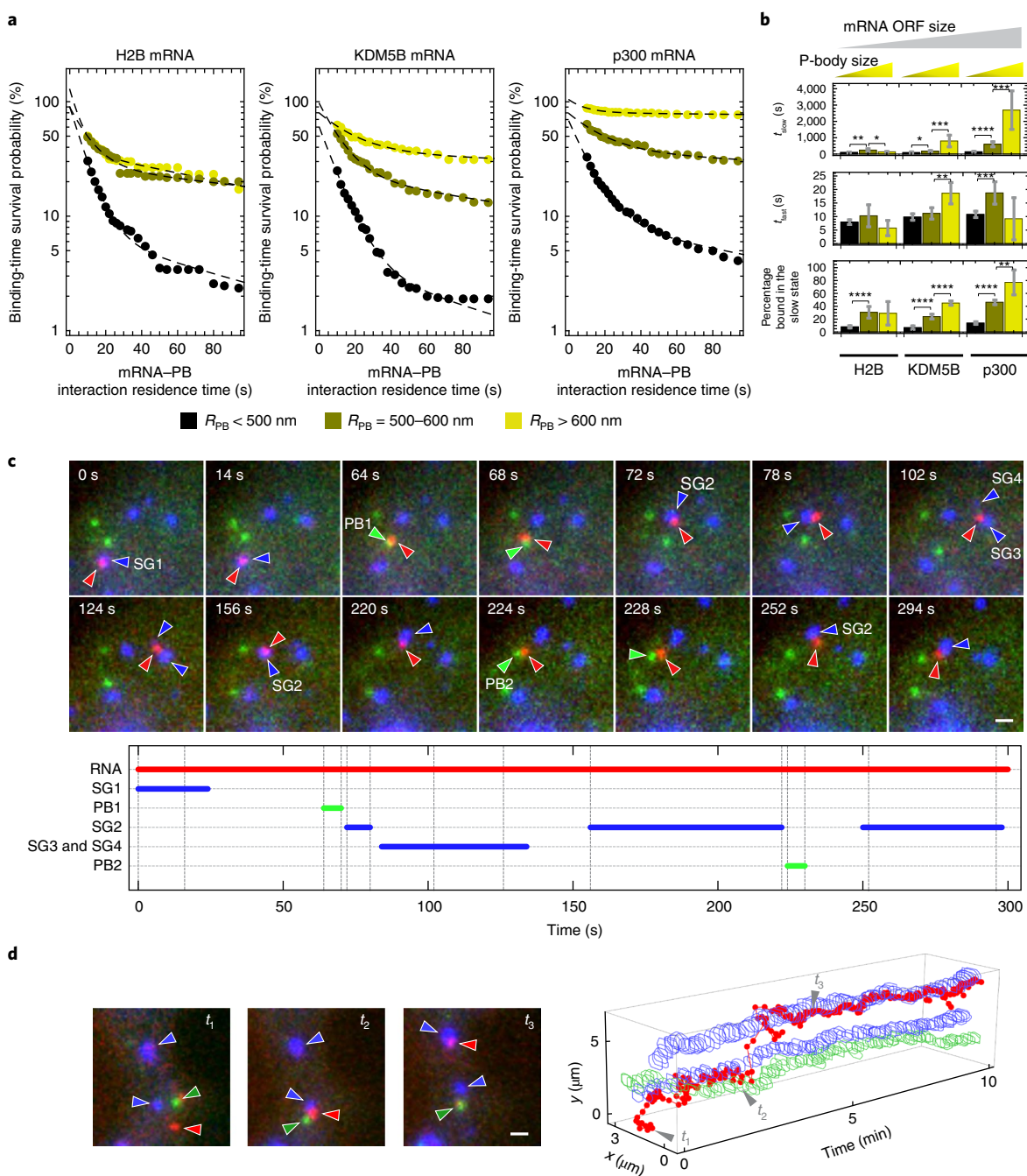
Fig. 3 | mRNAs interact transiently and stably with PBs in stressed cells and traffic bidirectionally between PBs and SGs. a, Average binding-time survival probability distributions of H2B mRNA–PB (left; data were calculated from 106 tracked PBs of $n = 4$ cells from one experiment), KDM5B mRNA–PB (middle; data were calculated from 137 tracked PBs of $n = 7$ cells collected from three independent experiments) and p300 mRNA–PB (right; data were calculated from 244 tracked PBs of $n = 16$ cells collected from four independent experiments) for a given effective PB radius (R_{PB}). **b**, The data in **a** were fit to a two-component model, resulting in average fitted fast (middle) and slow (top) interaction times; the percentage of mRNA bound to PBs in the slow interaction mode are shown. The fitted results are shown ($\pm$90% CI) for H2B, KDM5B and p300 mRNAs for each effective PB radius (legend in **a**). *$P < 0.05$, **$P < 0.01$, ***$P < 0.005$, ****$P < 0.001$, d.f. $= 31$; two-sided t-tests. The statistics source data can be found in Supplementary Table 2. Fitting was performed once to the collective data set shown in **a**. **c**, Representative images (top; from $n = 6$ cells collected from four independent experiments; scale bar, 1 µm) of a single KDM5B mRNA that interacted with four SGs and two PBs. The duration of each mRNA–RNP granule interaction was plotted (bottom). **d**, A representative mRNA trajectory (from $n = 3$ cells collected from two independent experiments) between two SGs and a PB visualized by plotting the position of the mRNA, SG and PB over time (right). Example cropped images corresponding to time points t_1 to t_3 are shown (left; scale bar, 1 µm). SGs, blue; mRNA, red and PB, green; the same colour codes apply to the arrows in **c**. The source data is provided in Supplementary Table 2.

interactions with SGs or PBs represent a low-valency interaction mode but provide a docked state whereby mRNPs can form additional interactions with SG components to perhaps enter a stable

locked state with higher valency (Fig. 4f). Higher valency would be expected on longer mRNAs and larger SGs or PBs, providing an explanation for why longer mRNAs and larger RNP granules have
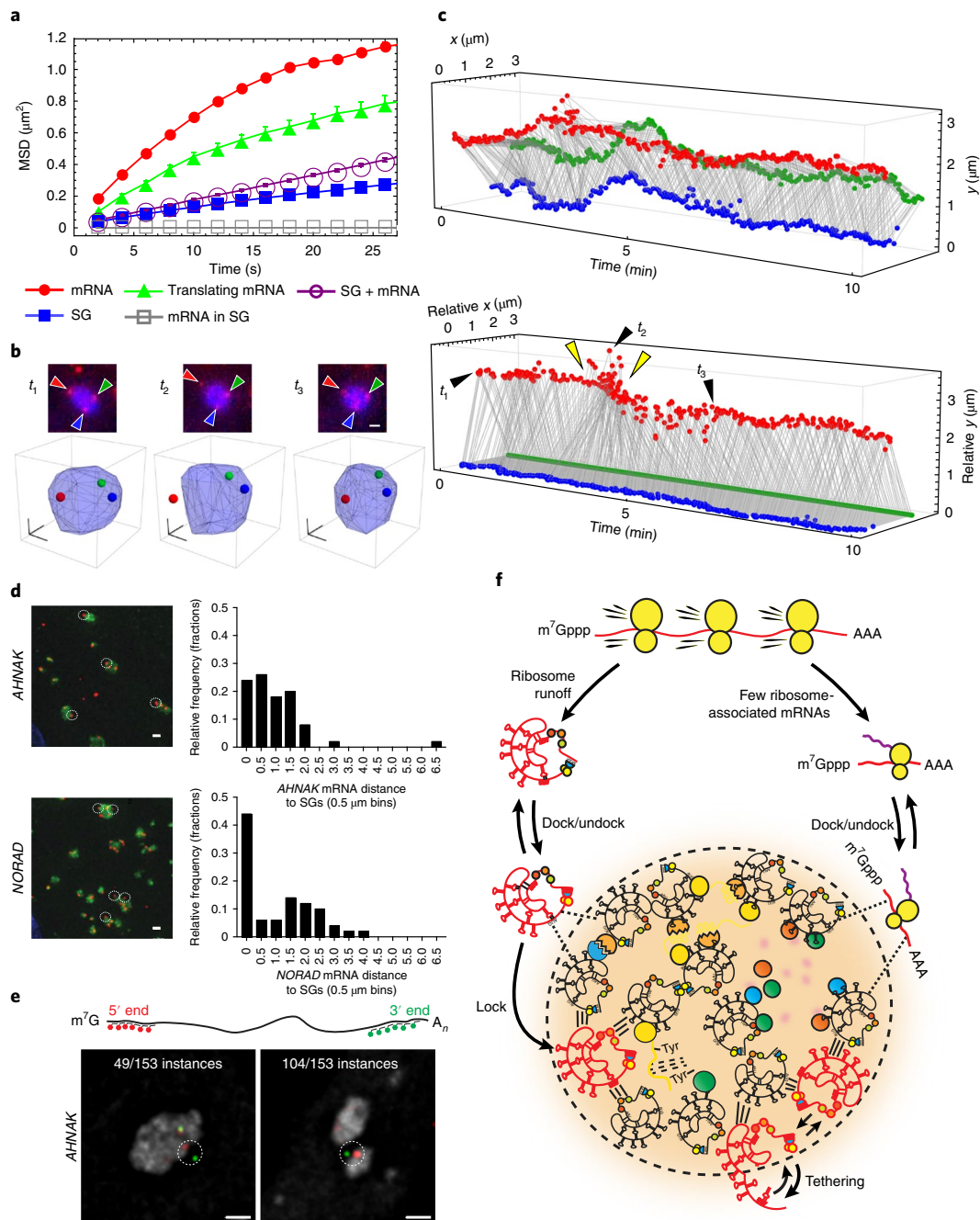
Fig. 4 | mRNAs can be rigidly positioned within SGs and/or tethered to them. a, Average mean squared displacement (MSD; $\pm 90\%$ CI) of cytoplasmic KDM5B mRNAs (fitted diffusion constant (D) = $0.016 \pm 0.004 \, \mu m^2 s^{-1}$), mRNAs with nascent chains (translating RNA; fitted $D = 0.011 \pm 0.002 \, \mu m^2 s^{-1}$), SGs (fitted $D = 0.003 \pm 0.0006 \, \mu m^2 s^{-1}$), SGs containing mRNAs (fitted $D = 0.004 \pm 0.0004 \, \mu m^2 s^{-1}$) and mRNAs in SGs (fitted $D = 10 \pm 2 \, nm^2 s^{-1}$) from $n = 7$ cells from two independent experiments; 1,243 mRNAs, 108 mRNAs with nascent chains, 1,049 SGs, and 92 SGs containing mRNAs were analysed, and 3 mRNAs were tracked in three dimensions (3D) within one SG. **b**, Representative time series (from $n = 2$ cells collected from two independent experiments) showing three KDM5B mRNAs (top; foci marked by red, blue and green arrows; scale bar, $1 \, \mu m$) and their 3D positions (bottom; red, green and blue dots) in a SG. **c**, Projected two-dimensional positions (top) and relative 3D positions (bottom) of the three mRNAs in **b** plotted over time (green mRNA position fixed and blue mRNA oriented relative to green mRNA). The frames in **b** t_1, t_2 and t_3 are indicated (black arrows). The yellow arrows indicate exit and entrance of the red mRNA from the SG (from $n = 2$ cells collected from two independent experiments). **d**, Representative immunofluorescence smFISH images of *AHNAK* ($n = 4$ cells) and *NORAD* ($n = 4$ cells) RNAs (red) and SGs (G3BP1, green) at 60 min post-arsenite stress (left); white circles indicate RNAs clustered near SGs. The images shown represent data from $n = 4$ cells collected from one experiment. Scale bar, $0.5 \, \mu m$. The relative frequency of distances of 50 *AHNAK* (top right) and *NORAD* (bottom right) RNAs to the nearest SG are shown. **e**, Schematic of *AHNAK* smFISH probe positions (top). Representative smFISH images where one end of the *AHNAK* mRNA was outside the SG while the other end was inside the SG are shown below. The 5′ probes are indicated in red, 3′ probes in green and SGs in grey; $n = 14$ cells collected from one experiment. Scale bars, $1 \, \mu m$. The source data is provided in Supplementary Table 2. **f**, Model depicting dynamic mRNA–SG interactions. Translation repression causes ribosomes to run off transcripts that can then interact transiently with SGs via docking and undocking. Some transcripts then enter a stable association (lock) with SGs and may engage in multivalent interactions with other RNAs and proteins. The transcripts may be tethered to the SG surface, possibly facilitating the growth of SGs or docking of PBs. The transcripts that remain in translation complexes can only transiently interact with SGs.

more stable RNA–granule interactions. Our experiments provide unambiguous evidence that mRNAs stably associated with SGs are translationally repressed, although mRNAs that are associated with polysomes can transiently interact with SGs. This may be because the 3′ untranslated region (UTR) and/or partially exposed coding regions may be sufficient to form transient protein–protein or RNA–RNA interactions, but a fully exposed coding region is required to make sufficient interactions for stable SG association. This work identifies the docking and locking steps as two distinct steps in RNP association with any RNP granule that can be modulated to affect RNA–granule association. We propose this bimodal nature of RNA–granule interaction as a general principle of any self-organized RNP granule where RNP recruitment requires entry into a multivalent state.

Online content

Any methods, additional references, Nature Research reporting summaries, source data, statements of data availability and associated accession codes are available at https://doi.org/10.1038/s41556-018-0263-4.

References

1. Buchan, J. R. & Parker, R. Eukaryotic stress granules: the ins and outs of translation. *Mol. Cell* **36**, 932–941 (2009).
2. Kedersha, N., Ivanov, P. & Anderson, P. Stress granules and cell signaling: more than just a passing phase? *Trends Biochem. Sci.* **38**, 494–506 (2013).
3. Schisa, J. A. Effects of stress and aging on ribonucleoprotein assembly and function in the germ line. *Wiley Interdisc. Rev. RNA* **5**, 231–246 (2014).
4. Sudhakaran, I. P. et al. FMRP and ataxin-2 function together in long-term olfactory habituation and neuronal translational control. *Proc. Natl Acad. Sci. USA* **111**, E99–E108 (2014).
5. El-Naggar, A. M. & Sorensen, P. H. Translational control of aberrant stress responses as a hallmark of cancer. *J. Pathol.* **244**, 650–666 (2018).
6. Grabocka, E. & Bar-Sagi, D. Mutant KRAS enhances tumor cell fitness by upregulating stress granules. *Cell* **167**, 1803–1813 (2016).
7. Zhang, K. et al. Stress granule assembly disrupts nucleocytoplasmic transport. *Cell* **173**, 958–971 (2018).
8. Neumann, M. et al. Ubiquitinated TDP-43 in frontotemporal lobar degeneration and amyotrophic lateral sclerosis. *Science* **314**, 130–133 (2006).
9. Li, Y. R., King, O. D., Shorter, J. & Gitler, A. D. Stress granules as crucibles of ALS pathogenesis. *J. Cell Biol.* **201**, 361–372 (2013).
10. Morisaki, T. et al. Real-time quantification of single RNA translation dynamics in living cells. *Science* **352**, 1425–1429 (2016).
11. Grimm, J. B. et al. A general method to improve fluorophores for live-cell and single-molecule microscopy. *Nat. Methods* **12**, 244–250 (2015).
12. Kedersha, N., Tisdale, S., Hickman, T. & Anderson, P. Real-time and quantitative imaging of mammalian stress granules and processing bodies. *Methods Enzymol.* **448**, 521–552 (2008).
13. Khong, A. et al. The stress granule transcriptome reveals principles of mRNA accumulation in stress granules. *Mol. Cell* **68**, 808–820 (2017).
14. Wheeler, J. R., Matheny, T., Jain, S., Abrisch, R. & Parker, R. Distinct stages in stress granule assembly and disassembly. *eLife* **5**, e18413 (2016).
15. Kedersha, N. et al. Dynamic shuttling of TIA-1 accompanies the recruitment of mRNA to mammalian stress granules. *J. Cell Biol.* **151**, 1257–1268 (2000).
16. Ohshima, D., Arimoto-Matsuzaki, K., Tomida, T., Takekawa, M. & Ichikawa, K. Spatio-temporal dynamics and mechanisms of stress granule assembly. *PLoS Comput. Biol.* **11**, e1004326 (2015).
17. Namkoong, S., Ho, A., Woo, Y. M., Kwakm, H. & Lee, J. H. Systematic characterization of stress-induced RNA granulation. *Mol. Cell* **70**, 175–187 (2018).
18. Wilbertz, J. H. et al. Single-molecule imaging of mRNA localization and regulation during the integrated stress response. *Mol. Cell* https://doi.org/10.1016/j.molcel.2018.12.006 (2019).
19. Kedersha, N. et al. Stress granules and processing bodies are dynamically linked sites of mRNP remodeling. *J. Cell Biol.* **169**, 871–884 (2005).
20. Simpson, C. E., Lui, J., Kershaw, C. J., Sims, P. F. G. & Ashe, M. P. mRNA localization to P-bodies in yeast is biphasic with many mRNAs captured in a late Bfr1p-dependent wave. *J. Cell Sci.* **127**, 1254–1262 (2014).
21. Wei, M.-T. et al. Phase behaviour of disordered proteins underlying low density and high permeability of liquid organelles. *Nat. Chem.* **9**, 1118–1125 (2017).
22. Feric, M. et al. Coexisting liquid phases underlie nucleolar subcompartments. *Cell* **165**, 1686–1697 (2016).
23. Molliex, A. et al. Phase separation by low complexity domains promotes stress granule assembly and drives pathological fibrillization. *Cell* **163**, 123–133 (2015).
24. Sfakianos, A. P., Whitmarsh, A. J. & Ashe, M. P. Ribonucleoprotein bodies are phased. *Biochem. Soc. Trans.* **44**, 1411–1416 (2016).
25. Niewidok, B. et al. Single-molecule imaging reveals dynamic biphasic partition of RNA-binding proteins in stress granules. *J. Cell Biol.* **217**, 1303–1318 (2018).
26. Banani, S. F. et al. Compositional control of phase-separated cellular bodies. *Cell* **166**, 651–663 (2016).

Author contributions

S.L.M. and R.P. conceptualized the study; S.L.M., T.M., T.J.S., A.K. and K.L. developed and designed methodology; T.M. and T.J.S. developed and implemented software; S.L.M. validated findings; T.M., T.J.S., S.L.M. and A.K. performed formal analyses; S.L.M., A.K., K.L., T.M. and T.J.S. performed experiments and/or collected data; R.P., T.J.S., T.M., A.K., K.L. and S.L.M. provided resources; T.M., T.J.S. and S.L.M. provided data curation; S.L.M. and R.P. wrote the original draft; R.P., S.L.M., T.J.S., T.M. and A.K. reviewed and edited the drafts; T.M., T.J.S., S.L.M. and A.K. visualized data; R.P., T.J.S., T.M. and S.L.M. supervised the project; S.L.M. managed and coordinated the project; T.J.S., R.P. and S.L.M. acquired funding.

Competing interests

The authors declare no competing interests.

Additional information

Supplementary information is available for this paper at https://doi.org/10.1038/s41556-018-0263-4.

Reprints and permissions information is available at www.nature.com/reprints.

Correspondence and requests for materials should be addressed to R.P. or T.J.S.

Publisher's note: Springer Nature remains neutral with regard to jurisdictional claims in published maps and institutional affiliations.

Methods

Cell culture. U-2 OS cells stably expressing the SG marker GFP–G3BP1 and the PB marker mRFP–DCP1a (a gift from the Kedersha lab[12]) were maintained in DMEM supplemented with 10% fetal bovine serum and 1% streptomycin/penicillin. Cells harbouring the GFP–G3BP1 SG marker alone were isolated by cell sorting of the GFP–G3BP1 and mRFP–DCP1 mixed cell pool (BioFrontiers Institute Flow Cytometry Core). U-2 OS cells were validated by STR (short tandem repeat) profiling and morphological assessments.

Fab generation and dye conjugation. Fab generation and dye conjugation were performed essentially as described by Morisaki and colleagues[10]. Briefly, a Pierce mouse IgG1 preparation kit (Thermo Scientific) was used to generate Fab according to the manufacturer's instructions. Immobilized ficin in the presence of 25 mM cysteine was used to digest FLAG (Wako, catalogue number 012-22384 anti-DYKDDDDK mouse IgG2b monoclonal) antibodies to create Fab. The Fabs were separated from the Fc region using NAb Protein A columns. After elution, the Fabs were concentrated to 1 mg ml^{-1} and conjugated to Cy3. Cy3 *N*-hydroxysuccinimide ester (Invitrogen) was dissolved in dimethylsulfoxide and stored at −20 °C. Fabs (100 µg) were diluted in 100 µl 100 mM NaHCO$_3$ (pH 8.5). Cy3 (1.33 µl) was added to this solution and incubated with end-over-end rotation for 1–2 h at room temperature. The conjugated Fabs were then eluted from a PBS pre-equilibrated PD-mini G-25 desalting column (GE Healthcare) that removed unconjugated dye. Conjugated Fabs were then concentrated using an Ultrafree 0.5 filter (10K nominal molecular weight limit; Millipore) to 1 mg ml^{-1}. The Fab to dye ratio was calculated using the absorbance at 280 and 550 nm ($A_{ratio,measured}$) and the extinction coefficient (ε) of Fab with the dye correction factor (CF) at 280 nm provided by the manufacturers (0.08 for Cy3). The degree of labelling (DOL) was calculated using the following formula:

$$DOL = \left(\frac{\varepsilon_{protein}}{\varepsilon_{dye}} \right) \left(\frac{1}{1/A_{ratio,measured} - CF} \right) \quad (1)$$

Only Fabs with a DOL of ~1 were used.

MCP purification. MCP was purified as described in Morisaki and colleagues[10]. His-tagged MCP was purified with Ni-NTA-agarose (Qiagen) following the manufacturer's instructions with minor modifications. Bacteria were lysed in a PBS-based buffer containing a complete set of protease inhibitors (Roche) and binding to the Ni-NTA resin was carried out in the presence of 10 mM imidazole. After washing with 20 and 50 mM imidazole in PBS, the protein was eluted with 300 mM imidazole in PBS and immediately used for experiments. The remainder was dialysed against a HEPES-based buffer (10% glycerol, 25 mM HEPES pH 7.9, 12.5 mM MgCl$_2$, 100 mM KCl, 0.1 mM EDTA, 0.01 % NP-40 detergent and 1 mM dithiothreitol) and stored at −80 °C after snap-freezing in liquid nitrogen.

Nascent chain tracking. Nascent chain tracking was done essentially as described by Morisaki and colleagues[10]. Briefly, a plasmid expressing a reporter mRNA encoding the FLAG spaghetti monster tag N-terminal to H2B (Addgene plasmid no. 81082), KDM5B (Addgene plasmid no. 81084) or p300 ORFs, followed by the 3′ UTR of beta-actin with 24× MS2 stem loops, was either transfected into cells 2 h before bead-loading or into cells together with purified Fab and/or MCP. Fluorescently labelled Fab (100 µg ml^{-1}) and/or purified MCP–HaloTag protein (33 µg ml^{-1}) in 4 µl PBS were bead loaded. Cells were incubated for 2–3 h in DMEM lacking phenol red with 10% fetal bovine serum, 1% streptomycin/penicillin and 1% glutamine before imaging. Cells were incubated for 30 min in the presence of JF646–HaloTag ligand to label the MCP–HaloTag protein and washed three times immediately before imaging.

Imaging conditions. To track single mRNAs and their translation status with RNP granules, we used a custom-built widefield fluorescence microscope with a highly inclined illumination scheme[10,27]. Briefly, the excitation beams, 488, 561 and 637 nm solid-state lasers (Vortran), were coupled and focused on the back focal plane of the objective (×60 numerical aperture 1.49 oil immersion objective, Olympus). The emission signals were split by an imaging grade, ultra-flat dichroic mirror (T660lpxr, Chroma) and detected by two aligned EM-CCD (iXon Ultra 888, Andor) cameras by focusing with 300 mm tube lenses (this lens combination produces 100× images with 130 nm pixel^{-1}).

Live cells were placed into an incubation chamber at 37 °C with 5% CO$_2$ (Okolab) on a piezoelectric stage (PZU-2150, Applied Scientific Instrumentation). The focus was maintained with the CRISP Autofocus System (CRISP-890, Applied Scientific Instrumentation). The lasers, cameras and piezoelectric stage were synchronized by an Arduino Mega board. Image acquisition was performed using the open source Micro-Manager software (1.4.22)[28,29]. The imaging size was set to 512×512 pixels^2 (66.6×66.6 µm^2) and the exposure time was selected as 53.64 ms. The readout time of the cameras from the combination of our imaging size and the vertical shift speed we selected was 23.36 ms, which resulted in an imaging rate of 13 Hz (70 ms per image). The excitation laser lines were digitally synced so that they illuminated the cells only when the camera was exposing, to avoid

any excess observational photobleaching. The far-red signal of mRNA visualized by JF646–MCP was imaged on one camera and the red signal of translation (or PBs) visualized by Cy3–FLAG–Fab (or mRFP–DCP1) and the green signal of SGs visualized by GFP–G3BP1 were imaged on the other camera. Cy3/mRFP and GFP signals were imaged alternately. To minimize the bleed through, the JF646 signal was simultaneously imaged with the GFP signal. We also employed a filter wheel (HS-625 HSFW TTL, Finger Lakes Instrumentation) equipped with a filter for Cy3 and mRFP (593/46 nm BrightLine, Semrock), and for GFP (510/42 nm BrightLine, Semrock). The filter position was changed during the camera read-out time (23.36 ms) by the Arduino Mega board.

To capture the entire thickness of the cytoplasm of U-2 OS cells, 13 z stacks of step size 500 nm (6 µm in total) were imaged using the piezoelectric stage so that the z position changed every two images (Cy3 and GFP). This resulted in our total cellular imaging rate of 0.5 Hz (2 s per volume). For Fig. 1b,e, the cells were first imaged at a single time point with 13 z stacks before arsenite addition (Time point 0). Arsenite was then added (0.5 mM) and after 10 min cells were imaged every 3 min with 13 z stacks per time point for up to 60 min. For Fig. 1f, image acquisitions were performed with the same conditions described above, except that the cells were washed with fresh media ten times at 70 min post-stress. Ten minutes after washout, cells were imaged again every 3 min with 13 z stacks per time point for another 60 min. For all other figures, the cells were imaged continuously at 0.5 Hz with 13 z stacks per time point for 10 min beginning between 10 and 30 min post-stress (when SGs were visible). Note that all of the colours described in the text and figures are based on the colour of excitation lasers as mentioned above, namely mRNA in red (JF646), translation or PB in green (Cy3 or mRFP) and SG in blue (GFP). Following this colour scheme, purple corresponds to mRNA (red) in SGs (blue), whereas yellow corresponds to mRNA in PBs and brown corresponds to translating mRNAs in SGs.

Analysis of SG formation, mRNA localization and translation. Single particle detection was performed on XY maximum projections of the stacks to detect mRNA, translation and SGs, using custom Mathematica code (version 11.2.0.0). Briefly, for each image channel, a bandpass filter was used to highlight particles within a given size range and the resulting image was binarized using a reasonable threshold to create a mask of the cell in which the vast majority of mRNA, translation or SGs were detectable. The Mathematica command ComponentMeasurements was then used to measure the intensity-centroid position, area, total intensity and convex vertices of each masked object, either mRNA, translation or SGs. The precise coordinates (super-resolved locations) of mRNAs and nascent peptides were determined by fitting (using the built-in Mathematica routine NonlinearModelFit) the original, pre-processed sub-images of the detected particles to two-dimensional Gaussians of the following form:

$$I(x, y) = I_{BG} + Ie^{-\frac{(x-x_0)^2}{2\sigma_x^2} - \frac{(y-y_0)^2}{2\sigma_y^2}}$$

where I_{BG} is the background fluorescence, I is the particle intensity, σ_x, σ_y are the spreads of the particle and x_0, y_0 represent the particle location. The offset between the two cameras was registered using the built-in Mathematica routine FindGeometricTransform to find the transform function that best aligned the fitted positions of 200 nm diameter Tetraspeck beads evenly spread out across the image field-of-view. Translating mRNAs were found by selecting mRNAs that colocalize with a translation signal location within 390 nm of the mRNA. Messenger RNAs within the SGs were found by selecting mRNAs within the detected SG-masked regions. The number of translating mRNAs in the cytosol or SGs, and the number of non-translating mRNAs in the cytosol or SGs were counted and divided by the total number of mRNAs at each time point to determine the fraction of each population throughout the time course during stress. The number of SGs was renormalized to the fraction of the maximum number of SGs detected in the cell at a single time point. As the timing of the beginning of SG formation varies from cell to cell, all of the the curves were aligned first before averaging the data from different cells. This alignment was done as follows. First, the SG formation curve was fit with the following equation:

$$N_{SG} = A \times \tanh(B \times t - C)$$

where N_{SG} is the number of SGs, A, B and C are normalization factors, and t is the frame number. Then, from the fitted results, all of the single-cell curves were shifted so that their values at 10% of their maxima were aligned. These aligned curves were then averaged.

Analysis of mRNA interactions with SGs and PBs. The location and the area of mRNA, SGs and PBs were detected and tracked as described above. The effective radius was then calculated from the area as the radius of an equivalent-area circle. Although the effective radius is a good approximation of the size of the object, it can be influenced by the brightness of the object as it is calculated from a binarized mask. Thus, small objects that are extremely bright (particularly PBs) may have effective radii that are a bit larger than they are in reality. The option 'CornerNeighbors → False' was used to prevent the detection of any SGs or

mRNAs that may have been clipped near the edge of the image frame. From these tracks and the binarized masks, the presence or absence of mRNA inside tracked SGs or PBs could be easily determined by the overlap of mRNA masks with the tracked SG or PB mask. The length of consecutive frames for which a tracked SG or PB mask had an overlapping mRNA mask was then set as equal to the length of the interaction time. Interactions that lasted for less than two frames (1 s) were ignored, as they could be influenced by imaging noise. If more than one mRNA mask overlapped with a SG or PB mask, it was counted as a single interaction (as most of the time these mRNA masks themselves overlapped, thus making it difficult to know how many mRNAs were actually present). This tends to slightly underestimate the number of long interactions. Finally, to validate our image analysis pipeline, we manually assessed the interaction times of individual KDM5B mRNAs in SGs and PBs using Fiji[30]. In all cases, manual measurements agreed well with the image analysis results in Mathematica.

To calculate the probability of an interaction lasting a certain amount of time (that is the survival probability of the interaction), we counted the fraction of tracks that lasted longer than N seconds, with N ranging from 6 to 300. A curve of the fraction of tracks versus time was then fit to a double exponential curve of the form $Ae^{-t/t_1} + Be^{-t/t_2}$. The data was then renormalized according to the fit so that at $t = 0$ s the fraction was 100% (that is $A + B = 100$). The renormalized data represents the survival probability versus time and is displayed in the plots in the main text along with the fitted fast interaction time t_1, slow interaction time t_2 and the slow fraction $B/(A + B)$. The 90% CI was calculated for the fitted values, from which the s.d. was estimated. From the s.d. and fitted mean values from each fit, effect size and P values between fits were calculated. All of the source data and information used to derive statistics are provided in Supplementary Table 2.

Analysis of MSD and 3D movement of mRNAs within SGs. The MSD was calculated using the tracked mRNA super-resolved locations for mRNA in the cytoplasm or in SGs. The MSD of mRNA inside SGs was calculated by dividing the MSD of the position of one mRNA with respect to the other by a factor of two. The MSD of SGs was calculated using the intensity-centroid of the SG.

The 3D coordinates of mRNAs were determined by fitting (using the built-in Mathematica routine NonlinearModelFit) the original, pre-processed sub-image stacks of the detected particle to 3D Gaussians of the following form:

$$I(x, y) = I_{BG} + Ie^{-\frac{(x-x_0)^2}{2\sigma_x^2} - \frac{(y-y_0)^2}{2\sigma_y^2} - \frac{(z-z_0)^2}{2\sigma_z^2}}$$

The convex vertices of SGs and the locations of mRNAs were plotted. For these analyses, mRNA spots were linked to the nearest neighbour mRNA in the consecutive frame. With the sparse mRNA density in the analysed SGs and the high temporal imaging frequency, it is unlikely that different mRNAs will be linked frame to frame. Additionally, the quality of automated tracking was validated by eye to ensure proper tracking.

Sequential immunofluorescence and smFISH. The protocol was performed as described previously[13]. Briefly, U-2 OS cells were seeded on sterilized coverslips in six-well tissue-culture plates. At ~80% confluency, the media was exchanged with fresh media 60 min before stress. Cells were then stressed with the addition of sodium arsenite (0.5 mM) for 60 min. Media was then removed and cells were washed with pre-warmed PBS. Cells were fixed for 10 min at room temperature with 500 μl 4% paraformaldehyde. After fixation, cells were washed twice with PBS, permeabilized in 0.1% Triton X-100 in PBS for 5 min and washed once with PBS. Coverslips were transferred to a humidifying chamber and cells were incubated in 5 μg ml⁻¹ mouse α-G3BP1 antibody (ab56574, Abcam) in PBS for 60 min at room temperature. The coverslips were next transferred to a 6-well plate and washed three times with PBS. The coverslips were then transferred back to the humidifying chamber and incubated in goat α-mouse FITC-conjugated antibody in PBS (1:1,000 dilution; ab6785, Abcam) for 60 min at room temperature. The coverslips were transferred to 6-well plate and washed three times with PBS. Antibodies that were bound to cells were fixed on cells by incubating the coverslips with 500 μl 4% paraformaldehyde for 10 min at room temperature.

After immunofluorescence, smFISH was performed as described previously[13], which was adapted from the protocol provided by Biosearch Technologies website[31]. Biosearch Technologies Stellaris Buffers were also used (SMF-HB1–10, SMF-WA1–60 and SMF-WB1–20). Specific smFISH probes were created by Biosearch Technologies. The probes to the 5′ end of the *AHNAK* mRNA and for *NORAD* were described in ref. [14]. The probes to the 3′ end of the *AHNAK* mRNA are described in Supplementary Table 1. Imaging was performed using a widefield DeltaVision Elite microscope with a ×100 objective and a PCO Edge sCMOS camera and softWoRx. The images shown in Fig. 4d were deconvolved and maximum intensity projections made from at least 30 z stacks to span the entire cell using Fiji[30]. Figure 4e shows images from a single z plane.

Image analysis with Bitplane Imaris analysis software. Image analysis of SGs and smFISH spots was conducted using Bitplane Imaris analysis software (8.4.1) as described previously[13]. To measure the distances between smFISH spots to the nearest SG, smFISH diffraction limited spots and SGs were first identified by Imaris imaging software using the spot and cell component, respectively. Recognition of the smFISH diffraction limited spot by the spot component was determined using the following parameters: diameter, 0.2 μm and thresholding, manually determined for each image. Recognition of SGs (G3BP1 staining) by the cell component was determined using the following parameters: minimum size, ≥1 voxel) and thresholding, manually determined for each image. A measuring tool (measuring points) was then manually applied to measure the distance between the centre of the spot and the surface of the SG. This was applied to 50 individual *NORAD* or *AHNAK* RNAs as described in Fig. 4d.

Statistics and reproducibility. For live cell imaging, all experiments were performed with at least ten cells collected from three or four independent experiments to account for cell-to-cell variability. Images were discarded if they were of insufficient quality to accurately analyse. The number of images that were deemed to be of sufficient quality for inclusion in each analysis are described below. For the mRNA–SG interaction experiments: H2B, data were calculated from 492 tracked SGs from 11 cells collected from 3 independent experiments; KDM5B, data were calculated from 409 tracked SGs from 9 cells collected from 4 independent experiments; p300, data were calculated from 824 tracked SGs from 16 cells from 4 independent experiments. For mRNA–PB interaction experiments: H2B, data were calculated from 106 tracked PBs of 4 cells from 1 experiment; KDM5B, data were calculated from 137 tracked PBs of 7 cells collected from 3 independent experiments; p300, data were calculated from 244 tracked PBs of 16 cells collected from 4 independent experiments. For fixed cell experiments, each cell was considered as an independent biological replicate. The smFISH experiments were performed once to detect *AHNAK* and once to detect *NORAD* and the distance of 50 *AHNAK* or 50 *NORAD* RNAs from the nearest SG was determined in four cells each. The analysis of *AHNAK* 5′ and 3′ ends within SGs and outside SGs was performed using data from one experiment, with 153 mRNAs analysed in 14 cells.

For live-cell imaging experiments, the s.e.m. representing variation between individual cells was calculated, except for Figs. 2d and 3b. Figures 2d and 3b were created using the fitted results from the plots in Figs. 2c and 3a, respectively. Each bar represents a fitted value and each error bar represents a 90% CI of the fit, calculated using Mathematica's built-in function NonlinearModelFit. The d.f. of the fits was 44 and 31 for Figs. 2d and 3b, respectively. The s.e.m. was calculated from the 90% confidence intervals (that is the 90% CIs were divided by 1.645), from which the two-sided *t*-test was performed and the *P* values were calculated.

Reporting Summary. Further information on research design is available in the Nature Research Reporting Summary linked to this article.

Code availability

Custom Mathematica (version 11.2.0.0) code was deposited on GitHub and can be accessed at https://raw.githubusercontent.com/TatsuyaMorisaki/Translation-Stress/master/Translation-Stress.nb.

Data availability

Source data for Figs. 1b–f, 2c–e, 3a–d, 4a,c–e and Supplementary Figs. 1,2,4 are provided in Supplementary Table 2. The raw images were deposited to figshare and can be accessed at: https://figshare.com/articles/Dataset_associated_with_Multicolor_single-molecule_tracking_of_mRNA_interactions_with_RNP_granules_-1_2/7427816 and https://figshare.com/articles/Dataset_associated_with_Multicolor_single-molecule_tracking_of_mRNA_interactions_with_RNP_granules_-2_2/7427918. All other data supporting the findings of this study are available from the corresponding authors on reasonable request.

References

27. Tokunaga, M., Imamoto, N. & Sakata-Sogawa, K. Highly inclined thin illumination enables clear single-molecule imaging in cells. *Nat. Methods* **5**, 159–161 (2008).
28. Edelstein, A. D. et al. Advanced methods of microscope control using μManager software. *J. Biol. Methods* **1**, e10 (2014).
29. Edelstein, A., Amodaj, N., Hoover, K., Vale, R. & Stuurman, N. Computer control of microscopes using μManager. *Curr. Protoc. Mol. Biol.* **29**, 14.20.1–14.20.17 (2010).
30. Schindelin, J. et al. Fiji: an open-source platform for biological-image analysis. *Nat. Methods* **9**, 676–682 (2012).
31. *Stellaris® RNA FISH: Protocol for Sequential IF + FISH in Adherent Cells* (Biosearch Technologies, 2015); https://biosearchassets.blob.core.windows.net/assets/bti_custom_stellaris_immunofluorescence_seq_protocol.pdf.

natureresearch

Corresponding author(s):   Roy Parker and Timothy J. Stasevich

Reporting Summary

Nature Research wishes to improve the reproducibility of the work that we publish. This form provides structure for consistency and transparency in reporting. For further information on Nature Research policies, see Authors & Referees and the Editorial Policy Checklist.

Statistical parameters

When statistical analyses are reported, confirm that the following items are present in the relevant location (e.g. figure legend, table legend, main text, or Methods section).

n/a	Confirmed	
☐	☒	The exact sample size (n) for each experimental group/condition, given as a discrete number and unit of measurement
☐	☒	An indication of whether measurements were taken from distinct samples or whether the same sample was measured repeatedly
☐	☒	The statistical test(s) used AND whether they are one- or two-sided *Only common tests should be described solely by name; describe more complex techniques in the Methods section.*
☒	☐	A description of all covariates tested
☒	☐	A description of any assumptions or corrections, such as tests of normality and adjustment for multiple comparisons
☐	☒	A full description of the statistics including central tendency (e.g. means) or other basic estimates (e.g. regression coefficient) AND variation (e.g. standard deviation) or associated estimates of uncertainty (e.g. confidence intervals)
☐	☒	For null hypothesis testing, the test statistic (e.g. F, t, r) with confidence intervals, effect sizes, degrees of freedom and P value noted *Give P values as exact values whenever suitable.*
☒	☐	For Bayesian analysis, information on the choice of priors and Markov chain Monte Carlo settings
☒	☐	For hierarchical and complex designs, identification of the appropriate level for tests and full reporting of outcomes
☐	☒	Estimates of effect sizes (e.g. Cohen's d, Pearson's r), indicating how they were calculated
☐	☒	Clearly defined error bars *State explicitly what error bars represent (e.g. SD, SE, CI)*

Our web collection on statistics for biologists may be useful.

Software and code

Policy information about availability of computer code

Data collection	Micro-Manager (1.4.22) and softWoRx (6.5.2)
Data analysis	Custom Mathematica code (11.2.0.0), Fiji ImageJ (1.51s) and Imaris Image Analysis Software (8.4.1)

For manuscripts utilizing custom algorithms or software that are central to the research but not yet described in published literature, software must be made available to editors/reviewers upon request. We strongly encourage code deposition in a community repository (e.g. GitHub). See the Nature Research guidelines for submitting code & software for further information.

Data

Policy information about availability of data

All manuscripts must include a data availability statement. This statement should provide the following information, where applicable:

- Accession codes, unique identifiers, or web links for publicly available datasets
- A list of figures that have associated raw data
- A description of any restrictions on data availability

All data are included in the manuscript and/or available upon request. All source data is presented in Table S4.

Field-specific reporting

Please select the best fit for your research. If you are not sure, read the appropriate sections before making your selection.

☒ Life sciences ☐ Behavioural & social sciences ☐ Ecological, evolutionary & environmental sciences

For a reference copy of the document with all sections, see nature.com/authors/policies/ReportingSummary-flat.pdf

Life sciences study design

All studies must disclose on these points even when the disclosure is negative.

Sample size	Fig 1a: Representative image from n=10 independent biological replicates (cells). Fig 1b: n=10 independent biological replicates (cells). Fig 1c: n=82 independent replicates (non-translating mRNAs tracked). Fig 1d: n=334 independent replicates (translating mRNAs tracked). Fig 1e: n=10 independent biological replicates (cells). Fig 1f: n=4 independent biological replicates (cells). Fig 2c&d: H2B, n=11 independent biological replicates (cells) and 492 tracked SGs; KDM5B,n=9 biologically independent samples (cells) and 409 tracked SGs; p300, n=16 independent biological replicates (cells) and 824 tracked SGs. Fig 2e: KDM5B, n=10 independent biological replicates (cells) and 326 tracked SGs; p300, n=10 independent biological replicates, 336 tracked SGs. Fig3a&b: H2B, n=4 independent biological replicates (cells) and 106 tracked PBs; KDM5B, n=7 independent biological replicates (cells), 137 tracked PBs; p300, n=16 independent biological replicates (cells), 244 tracked PBs. Fig3c: n=6 independent biological replicates (cells). Fig3d: n=3 independent biological replicates (cells). Fig 4a: n=7 independent biological replicates (cells), 1243 mRNAs, 108 mRNAs with nascent chains, 1049 SGs, 92 SGs containing mRNAs and 3 mRNAs tracked in 3D within one SG (3D analysis of mRNA MSDs within one representative SG out of n=2 independent observations). Fig4b: Representative images shown from n=2 3D analyses of biologically independent samples. Fig 4c: Representative time series plotted from one representative SG out of n=2 3D analyses of biologically independent samples 300 time points analyzed. Fig 4d: n=4 independent biological replicates (cells) for AHNAK and n=4 independent biological replicates (cells) for NORAD. Fig 4e: n=14 independent biological replicates (cells) and 50 AHNAK mRNAs analyzed. All other figure panels are schematic or representative data to show examples. Additional examples are shown as Supplementary Figures.
Data exclusions	We excluded movies of cells that expressed too many reporter mRNAs because each mRNA cannot be tracked in these scenarios. We also excluded movies of cells that did not form stress granules because our focus is studying mRNA translation status and mobility in the context of stress granule formation.
Replication	We confirmed reproducibility by performing at least 3 independent experimental replicates for each assay. The 3D analysis of mRNAs within SGs required observing at least three distinct mRNA particles in one stress granule at the beginning of the 10 minute imaging timecourse (such that they could be independently tracked). These parameters were stringent enough that we could only analyze two SGs out of n=9 independent biological replicates (cells) containing a total of 409 trackable SGs.
Randomization	This is not relevant to our study as we automated the analysis of microscopy data in an unbiased manner. We used consistent thresholding for mRNA and RNP granule detection for each experiment.
Blinding	We used consistent thresholds to detect mRNAs and SGs throughout all experimental conditions. Following detection, analysis was fully automated such that there was no bias from the experimenter involved.

Reporting for specific materials, systems and methods

Materials & experimental systems

n/a	Involved in the study
☒	☐ Unique biological materials
☐	☒ Antibodies
☐	☒ Eukaryotic cell lines
☒	☐ Palaeontology
☒	☐ Animals and other organisms
☒	☐ Human research participants

Methods

n/a	Involved in the study
☒	☐ ChIP-seq
☒	☐ Flow cytometry
☒	☐ MRI-based neuroimaging

Antibodies

Antibodies used	1. Anti-DYKDDDDK antibody: Manufacturer: Wako, Catalog number: 012-22384, Clone No. 1E6, Lot number: SAN4130. 100 micrograms/mL of fluorescently labeled antibody fragment was used for each assay. 2. Anti-G3BP1 antibody: Manufacturer: Abcam, Catalog number: ab56574, Lot number: GR3193680-2, used at 5 micrograms/mL for immunofluorescence microscopy. 3. Goat α-Mouse FITC: Manufacturer: Abcam, Catalog number: ab6785, Lot number: GR247029-17, Used at 1:1000 dilution for immunofluorescence microscopy.
Validation	1. We generated FLAG Fab fragments by digesting anti-DYKDDDDK antibody, and validated its functionality as described in Morisaki et al (Science 2016). 2. Anti-G3BP1 antibody was validated for immunofluorescence staining and western blotting using human cells and cell lysates in our laboratory and by the manufacturer (https://www.abcam.com/g3bp-antibody-ab56574.html).

Eukaryotic cell lines

Policy information about cell lines

Cell line source(s)	U-2 OS cells from ATCC, GFP-G3BP1/mRFP-DCP1a U-2 OS cells from Dr Nancy Kedersha.
Authentication	U-2 OS cells were authenticated by STR profiling (ATCC) and morphological assessments.
Mycoplasma contamination	We confirmed that all cell lines tested negative for mycoplasma contamination.
Commonly misidentified lines (See ICLAC register)	No Commonly misidentified lines were used.